FILTERED-COPHY: UNSUPERVISED LEARNING OF COUNTERFACTUAL PHYSICS IN PIXEL SPACE

Anonymous authors
Paper under double-blind review

ABSTRACT

Learning causal relationships in high-dimensional data (images, videos) is a hard task, as they are often defined on low dimensional manifolds and must be extracted from complex signals dominated by appearance, lighting, textures and also spurious correlations in the data. We present a method for learning counterfactual reasoning of physical processes in pixel space, which requires the prediction of the impact of interventions on initial conditions. Going beyond the identification of structural relationships, we deal with the challenging problem of forecasting raw video over long horizons. Our method does not require the knowledge or supervision of any ground truth positions or other object or scene properties. Our model learns and acts on a suitable hybrid latent representation based on a combination of dense features, sets of 2D keypoints and an additional latent vector per keypoint. We show that this better captures the dynamics of physical processes than purely dense or sparse representations. We introduce a new challenging and carefully designed counterfactual benchmark for predictions in pixel space and outperform strong baselines in physics-inspired ML and video prediction.

1 INTRODUCTION

Reasoning on complex, multi-modal and high-dimensional data is a natural ability of humans and other intelligent agents (Martin-Ordas et al., 2008), and one of the most important and difficult challenges of AI. While machine learning is well suited for capturing regularities in high-dimensional signals, in particular by using high-capacity deep networks, some applications also require an accurate modeling of causal relationships. This is particularly relevant in physics, where causation is considered as a fundamental axiom. In the context of machine learning, correctly capturing or modeling causal relationships can also lead to more robust predictions, in particular better generalization to out-of-distribution samples, indicating that a model has overcome the exploitation of biases and shortcuts in the training data. In recent literature on physics-inspired machine learning, causality has often been forced through the addition of prior knowledge about the physical laws that govern the studied phenomena, e.g. (Yin et al., 2021). A similar idea lies behind structured causal models, widely used in the causal inference community, where domain experts model these relationships directly in a graphical notation. This particular line of work allows to perform predictions beyond statistical forecasting, for instance by predicting unobserved counterfactuals, the impact of unobserved interventions (Balke & Pearl, 1994) — "*What alternative outcome would have happened, if the observed event X had been replaced with an event Y (after an intervention)*". Counterfactuals are interesting, as causality intervenes through the effective modification of an outcome. As an example, taken from (Schölkopf et al., 2021), an agent can identify the direction of a causal relationship between an umbrella and rain from the fact that removing an umbrella will not affect the weather.

We focus on counterfactual reasoning on high-dimensional signals, in particular videos of complex physical processes. Learning such causal interactions from data is a challenging task, as spurious correlations are naturally and easily picked up by trained models. Previous work in this direction was restricted to discrete outcomes, as in *CLEVRER* (Yi et al., 2020), or to the prediction of 3D trajectories, as in *CoPhy* (Baradel et al., 2020), which also requires supervision of object positions. In this work, we address the hard problem of predicting the alternative (counterfactual) outcomes of physical processes in pixel space, i.e. we forecast sequences of 2D projective views of the 3D scene, requiring the prediction over long horizons (150 frames corresponding to $\sim$ 6 seconds). We conjecture that causal relationships can be modeled on a low dimensional manifold of the data,

and propose a suitable latent representation for the causal model, in particular for the estimation of the confounders and the dynamic model itself. Similar to V-CDN (Kulkarni et al., 2019; Li et al., 2020), our latent representation is based on the unsupervised discovery of keypoints, complemented by additional information in our case. Indeed, while keypoint-based representations can easily be encoded from visual input, as stable mappings from images to points arise naturally, we claim that they are not the most suitable representation for dynamic models. We identified and addressed two principal problems: (i) the individual points of a given set are discriminated through their 2D positions only, therefore shape, geometry and relationships between multiple moving objects need to be encoded through the relative positions of points to each other, and (ii) the optimal representation for a physical dynamic model is not necessarily a 2D keypoint space, where the underlying object dynamics has also been subject to the imaging process (projective geometry).

We propose a new counterfactual model, which learns a sparse representation of visual input in the form of 2D keypoints coupled with a (small) set of coefficients per point modeling complementary shape and appearance information. Confounders (object masses and initial velocities) in the studied problem are extracted from this representation, and a learned dynamic model forecasts the entire trajectory of these keypoints from a single (counterfactual) observation. Building on recent work in data-driven analysis of dynamic systems (Janny et al., 2021; Peralez & Nadri, 2021), the dynamic model is presented in a higher-dimensional state space, where dynamics are less complex. We show, that these design choices are key to the performance of our model, and that they significantly improve the capability to perform long-term predictions. Our proposed model outperforms strong baselines for physics-informed learning of video prediction.

We introduce a new challenging dataset for this problem, which builds on *CoPhy*, a recent counterfactual physics benchmark (Baradel et al., 2020). We go beyond the prediction of sequences of 3D positions and propose a counterfactual task for predictions in pixel space after interventions on initial conditions (displacing, re-orienting or removing objects). In contrast to the literature, our benchmark also better controls for the identifiability of causal relationships and counterfactual variables and provides more accurate physics simulation.

2 Related Work

Counterfactual (CF) reasoning — and learning of causal relationships in ML was made popular by works of J. Pearl, e.g. (Pearl, 2000), which motivate and introduce mathematical tools detailing the principles of *do-calculus*, i.e. study of unobserved interventions on data. A more recent survey links these concepts to the literature in ML (Schölkopf et al., 2021). The last years have seen the emergence of several benchmarks for CF reasoning in physics. CLEVRER (Yi et al., 2020) is a visual question answering dataset, where an agent is required to answer a CF question after observing a video showing 3D objects moving and colliding. Li et al. (2020) introduce a CF benchmark with two tasks: a scenario where balls interact with each other according to unknown interaction laws (such as gravity or elasticity), and a scenario where clothes are folded by the wind. The agent needs to identify CF variables and causal relationships between objects, and to predict future frames. CoPhy (Baradel et al., 2020) clearly dissociates the observed experiment from the CF one, and contains three complex 3D scenarios involving rigid body dynamics. However, the proposed method relies on the supervision of 3D object positions, while our work does not require any meta data.

Physics-inspired ML — and learning visual dynamics has been dealt early on with recurrent models (Srivastava et al., 2015; Finn et al., 2016; Lu et al., 2017), or GANs (Vondrick et al., 2016; Mathieu et al., 2016). Kwon & Park (2019) adopt a Cycle-GAN with two discriminator heads, in charge of identifying false images and false sequences in order to improve the temporal consistency of the model in long term prediction. Nonetheless, the integration of causal reasoning and prior knowledge in these models is not straightforward. Typical work in physics-informed models relies on disentanglement between physics-informed features and residual features (Villegas et al., 2017a; Denton & Birodkar, 2017) and may incorporate additional information based on the available priors on the scene (Villegas et al., 2017b; Walker et al., 2017). PhyDNet Le Guen & Thome (2020) explicitly disentangles visual features from dynamical features, which are supposed to follow a PDE. It achieves SOTA performance on Human3.6M (Ionescu et al., 2014) and Sea Surface Temperature (de Bezenac et al., 2018), but we show that it fails on our challenging benchmark.

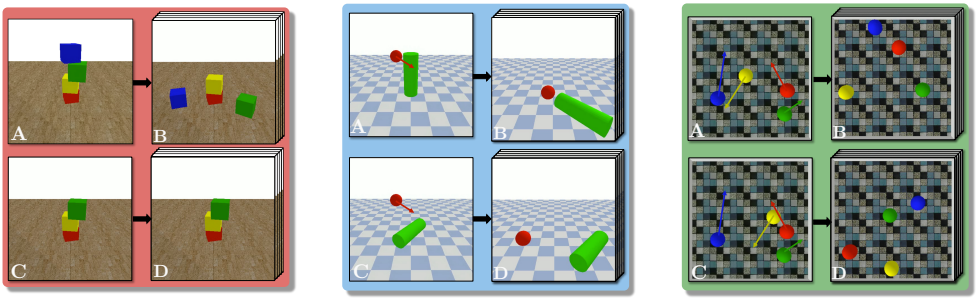

(a) `BlocktowerCF` (b) `CollisionCF` (c) `BallsCF`

Figure 1: The Filtered-CoPhy benchmark suite contains three challenging scenarios involving 2D or 3D rigid body dynamics with complex interactions, including collision and resting contact. Initial conditions $\mathbf{A}$ are modified to $\mathbf{C}$ by an intervention. Initial motion is indicated through arrows.

Keypoint detection — is a well researched problem in vision with widely used handcrafted baselines (Lowe, 1999). New unsupervised variants emerged recently and have been shown to provide a suitable object-centric representation, close to attention models, which simplify the use of physical and/or geometric priors (Locatello et al., 2020; Veerapaneni et al., 2020). They are of interest in robotics and reinforcement learning, where a physical agent has to interact with objects (Kulkarni et al., 2019; Manuelli et al., 2020; 2019). KeypointsNet (Suwajanakorn et al., 2018) is a geometric reasoning framework, which discovers meaningful keypoints in 3D through spatial coherence between viewpoints. Close to our work, (Minderer et al., 2019) proposes to learn a keypoints-based stochastic dynamic model. However, the model is not suited for CF reasoning in physics and may suffer from inconsistency in the prediction of dynamics over long horizons.

3 THE FILTERED-COPHY BENCHMARK

We build on *CoPhy* (Baradel et al., 2020), retaining its strengths, but explicitly focusing on a counterfactual scenario in pixel space and eliminating the ill-posedness of tasks we identified in the existing work. Each data sample is called an *experiment*, represented as a pair of trajectories: an *observed* one with initial condition $X_0 = \mathbf{A}$ and outcome $X_{t=1..T} = \mathbf{B}$ (a sequence), and a *counterfactual* one $\bar{X}_0 = \mathbf{C}$ and $\bar{X}_{t=1..T} = \mathbf{D}$ (a sequence). Throughout this paper we will use the letters $\mathbf{A}, \mathbf{B}, \mathbf{C}$ and $\mathbf{D}$ to distinguish the different parts of each experiment. The initial conditions $\mathbf{A}$ and $\mathbf{C}$ are linked through a *do-operator* $do(X_0 = \mathbf{C})$, which modifies the initial condition (Pearl, 2018). Experiments are parameterized by a set of intrinsic physical parameters z which are not observable from a single initial image $\mathbf{A}$. We refer to these as *confounders*. As in *CoPhy*, in our benchmark the do-operator is observed during training, but confounders are not — they have been used to generate the data, but are not used during training or testing. Following (Pearl, 2018), the counterfactual task consists in inferring the counterfactual outcome $\mathbf{D}$ given the observed trajectory $\mathbf{AB}$ and the counterfactual initial state $\mathbf{C}$, following a three-step process:

① **Abduction**: use the observed data $\mathbf{AB}$ to compute the counterfactual variables, i.e. physical parameters, which are not affected by the do-operation.

② **Action**: update the causal model; keep the same identified confounders and apply the do-operator, i.e. replace the initial state $\mathbf{A}$ by $\mathbf{C}$.

③ **Prediction** : Compute the counterfactual outcome $\mathbf{D}$ using the causal graph.

The benchmark contains three scenarios involving rigid body dynamics. `BlocktowerCF` studies stable and unstable 3D cube towers, the confounders are masses. `BallsCF` focuses on 2D collisions between moving spheres (confounders are masses and initial velocities). `CollisionCF` is about collisions between a sphere and a cylinder (confounders are masses and initial velocities) (Fig. 1).

Unlike *CoPhy*, our benchmark involves predictions in RGB pixel space only. The do-operation consists in visually observable interventions on $\mathbf{A}$, such as moving or removing an object. The confounders cannot be identified from the single-frame observation $\mathbf{A}$, identification requires the analysis of the entire $\mathbf{AB}$ trajectory.

Identifiability of confounders — For an experiment $(\mathbf{AB}, \mathbf{CD}, z)$ to be well-posed, the confounders z must be retrievable from $\mathbf{AB}$. For example, since the masses of a stable cube tower cannot be identified generally in all situations, it can be impossible to predict the counterfactual outcome of an unstable tower, as collisions are not resolvable without known masses. In contrast to *CoPhy*, we ensure that each experiment is well posed by applying the following constraint during generation. Let $\psi : (X_0, z) \mapsto X_{t=1..T}$ be the experiment, given initial condition X_0 and confounders z. Each experiment in **Filtered-CoPhy** satisfies the constraints defined below:

Definition 1 *(Identifiability, (Pearl, 2018)) The experiment* $(\mathbf{AB}, \mathbf{CD}, z)$ *is identifiable if, for any set of confounders* z'*:*

$$\psi(\mathbf{A}, z) = \psi(\mathbf{A}, z') \Rightarrow \psi(\mathbf{C}, z) = \psi(\mathbf{C}, z'). \tag{1}$$

In other words, an identifiable experiment guarantees that there is no pair (z, z') that gives the same trajectory $\mathbf{AB}$ but a different counterfactual outcome $\mathbf{CD}$. Details on how this constraint was enforced and on its impact on the estimation of confounders are given in appendix A.1.

Counterfactuality — We enforce sufficient difficulty of the problem through the meaningfulness of confounders. We remove initial situations where the choice of confounder values has no significant impact on the final outcome:

Definition 2 *(Counterfactuality). Let* z^k *be the set of confounders* z*, where the* k^{th} *value has been modified. The experiment* $(\mathbf{AB}, \mathbf{CD}, z)$ *is counterfactual if and only if:*

$$\exists k : \psi(\mathbf{C}, z^k) \neq \psi(\mathbf{C}, z). \tag{2}$$

In other words, we impose the existence of an object of the scene for which the (unobserved) physical properties have a determining effect on the trajectory. Details on how this constraint was enforced are given in appendix A.2.

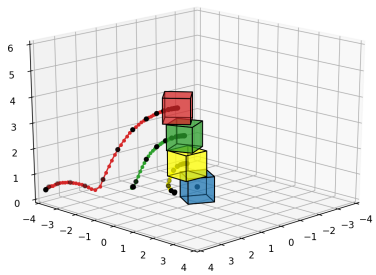

Figure 2: Impact of temporal frequency on dynamics, 3D trajectories of each cube are shown. Black dots are sampled at 5 FPS, colored dots at 25 FPS. Collisions between the red cube and the ground are not well described by the black dots, making it hard to infer physical laws from regularities in data.

Temporal resolution — the physical laws which govern **Filtered-CoPhy** involve highly non-linear phenomena, in particular collision and resting contacts. Collisions are difficult to learn because their actions are both intense, brief, and highly non-linear, depending on the geometry of the objects in 3D space. The temporal resolution of physical simulations is of prime importance. A parallel can be made with Nyquist-Shannon frequency, as a trajectory sampled with too low frequency cannot be reconstructed with precision. We simulate and record trajectories at 25 FPS, compared to 5 FPS chosen in *CoPhy*, justified with two experiments. Firstly, Fig. 2 shows the trajectories of the center of masses of cubes in `BlocktowerCF`, colored dots are shown at 25 FPS and black dots at 5 FPS. We can see that collisions with the ground fall below the sampling rate of 5 FPS, making it hard to infer physical laws from regularities in data at this frequency. A second experiment involves learning a prediction model at different frequencies, confirming the choice 25 FPS — details are given in appendix A.3.

4 Unsupervised Learning of Counterfactual Physics

We introduce a new model for counterfactual learning of physical processes capable of predicting visual sequences $\mathbf{D}$ in the image space over long horizons. The method does not require any supervision other than videos of observed and counterfactual experiences. The code is publicly available online at **https://filteredcophy.github.io**. The model consists of three parts, learning the latent representation and its (counterfactual) dynamics:

- **The encoder (De-Rendering module)** learns a hybrid representation of an image in the form of a (i) dense feature map and (ii) 2D keypoints combined with (iii) a low-dimensional vector of coefficients, see Fig. 3. Without any state supervision we show that the model learns a representation which encodes positions in keypoints and appearance and orientation in the coefficients.

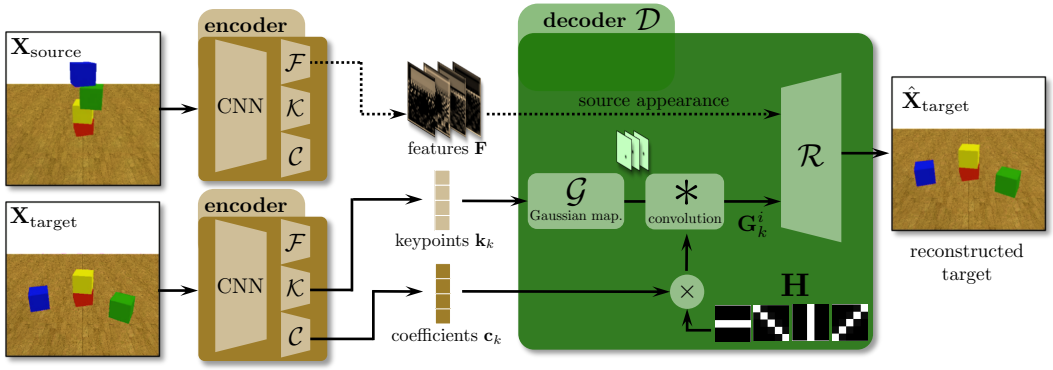

Figure 3: We de-render visual input into a latent space composed of a dense feature map $\mathbf{F}$ modeling static information, a set of keypoints $\mathbf{k}$, and associated coefficients $\mathbf{c}$. We here show the training configuration taking as input pairs $(\mathbf{X}_{\text{source}}, \mathbf{X}_{\text{target}})$ of images. Without any supervision, a tracking strategy emerges naturally through the unsupervised objective: we optimize reconstruction of $\mathbf{X}_{\text{target}}$, given features from $\mathbf{X}_{\text{source}}$ and keypoints+coefficients from $\mathbf{X}_{\text{target}}$.

- **The Counterfactual Dynamic (CoDy) model** based on recurrent graph networks, in the lines of (Baradel et al., 2020). It estimates a latent representation of the confounders z from the keypoint + coefficient trajectories of $\mathbf{AB}$ provided by the encoder, and then predicts $\mathbf{D}$ in this same space.
- **The decoder** that uses the predicted keypoints to generate a pixel-space representation of $\mathbf{D}$.

4.1 Disentangling visual information from dynamics

The encoder takes an input image $\mathbf{X}$ and predicts a representation with three different streams, sharing a common convolutional backbone, as shown in Fig. 3. We propose an unsupervised training objective, which favors the emergence of a suitable latent representation disentangling static and dynamic information.

1. A dense feature map $\mathbf{F} = \mathcal{F}(\mathbf{X})$, which contains static information, such as the background.
2. A set of 2D keypoints $\mathbf{k} = \mathcal{K}(\mathbf{X})$, which carry positional information from moving objects.
3. A set of corresponding coefficients $\mathbf{c} = \mathcal{C}(\mathbf{X})$, one vector $\mathbf{c}_k$ of size C per keypoint k, which encodes orientation and appearance information.

The unsupervised objective is formulated on pairs of images $(\mathbf{X}_{\text{source}}, \mathbf{X}_{\text{target}})$ randomly sampled from same $\mathbf{D}$ sequences (see appendix D.1 for details on sampling). Exploiting an assumption on the absence of camera motion[1], the goal is to favor the emergence of disentangling static and dynamic information. To this end, both images are encoded, and the reconstruction of the target image is predicted with a decoder $\mathcal{D}$ fusing the source dense feature map and the target keypoints and coefficients. This formulation requires the decoder to aggregate dense information from the source and sparse values from the target, naturally leading to motion being predicted by the latter.

On the decoder $\mathcal{D}$ side, we add inductive bias, which favors the usage of the 2D keypoint information in a spatial way. The 2D coordinates $\mathbf{k}_k$ for each keypoint k are encoded as Gaussian heatmaps $\mathcal{G}(\mathbf{k}_k)$, i.e. 2D Gaussian functions centered on the keypoint position. The additional coefficient information, carrying appearance information, is then used to deform the Gaussian mapping into an anisotropic shape using a fixed filter bank $\mathbf{H}$, as follows:

$$\mathcal{D}(\mathbf{F}, \mathbf{k}, \mathbf{c}) = \mathcal{R}\left(\mathbf{F}, \mathbf{G}_1^1, ..., \mathbf{G}_1^C, \mathbf{G}_2^1, ..., \mathbf{G}_K^C\right), \quad \mathbf{G}_k^i = \mathbf{c}_k^{C+1} \mathbf{c}_k^i \left(\mathcal{G}(\mathbf{k}_k) * \mathbf{H}_i\right), \tag{3}$$

where $\mathcal{R}(...)$ is a refinement network performing trained upsampling with transposed convolutions, whose inputs are stacked channelwise. $\mathbf{G}_k^i$ are Gaussian mappings produced from keypoint positions $\mathbf{k}$, deformed by filters from bank $\mathbf{H}$ and weighted by coefficients $\mathbf{c}_k^i$. The filters $\mathbf{H}_i$ are defined as

[1] If this assumption is not satisfied, global camera motion could be compensated after estimation.

fixed horizontal, vertical and diagonal convolution kernels. This choice is discussed in section 5. The joint encoding and decoding pipeline is illustrated in Fig. 3.

The model is trained to minimize the mean squared error (MSE) reconstruction loss, regularized with a loss on spatial gradients $\nabla \mathbf{X}$ weighted by hyper-parameters $\gamma_1, \gamma_2 \in \mathbb{R}$:

$$\mathcal{L}_{\text{deren}} = \gamma_1 \left|\left| \mathbf{X}_{\text{target}} - \hat{\mathbf{X}}_{\text{target}} \right|\right|_2^2 + \gamma_2 \left|\left| \nabla \mathbf{X}_{\text{target}} - \nabla \hat{\mathbf{X}}_{\text{target}} \right|\right|_2^2, \tag{4}$$

where $\hat{X}_{\text{target}} = \mathcal{D}(\mathcal{F}(\mathbf{X}_{\text{source}}), \mathcal{K}(\mathbf{X}_{\text{target}}), \mathcal{C}(\mathbf{X}_{\text{target}}))$ is the reconstructed image, γ_1 and γ_2 are scalar weights.

Related work – our unsupervised objective is somewhat related to *Transporter* (Kulkarni et al., 2019), which, as our model, computes visual feature vectors F_{source} and F_{target} as well as 2D keypoints K_{source} and K_{target}, modeled as a 2D vector via Gaussian mapping. It then leverages a handcrafted transport equation for reconstruction: $\hat{\Psi}_{\text{target}} = F_{\text{source}} \times (1 - K_{\text{source}}) \times (1 - K_{\text{target}}) + F_{\text{target}} \times K_{\text{target}}$. As in our case, the target image is reconstructed through a refiner network $\hat{X}_{\text{target}} = \mathcal{R}(\hat{\Psi}_{\text{target}})$. The transporter suffers from a major drawback when used for the targeted application, video prediction, as it requires parts of the target image to reconstruct the target image — the model was originally proposed in the context of RL and control, where image reconstruction is not a main objective. The transporter also uses keypoints without shape coefficients, requiring object shapes to be encoded by several keypoints, or abusively be carried through the dense features F_{target}. This typically leads to complex dynamics non representative of the dynamical objects. We conducted an in-depth comparison between the Transporter and our proposed representation in appendix C.2.

4.2 Dynamic model and confounder estimation

Our counterfactual dynamic model (CoDy) leverages multiple graph network (GN) based modules (Battaglia et al., 2016) that join forces to solve the counterfactual forecasting tasks of **Filtered-CoPhy**. Each one of these networks is a classical GN, abbreviated as $\mathcal{GN}(\mathbf{x}_k)$, which contextualizes input node embeddings $\mathbf{x}_k$ through incoming edge interactions $\mathbf{e}_{ik}$, providing output node embeddings $\hat{\mathbf{x}}_k$ (parameters are not shared over the instances):

$$\mathcal{GN}(\mathbf{x}_k) = \hat{\mathbf{x}}_k, \text{ such that } \hat{\mathbf{x}}_k = g\left(\mathbf{x}_k, \sum_i \mathbf{e}_{ik}\right) \text{ with } \mathbf{e}_{ij} = f\left(\mathbf{x}_i, \mathbf{x}_j\right), \tag{5}$$

where f is a message-passing function and g is an aggregation function.

We define the state of frame $\mathbf{X}_t$ at time t as a stacked vector composed of keypoints and coefficients computed by the encoder (the de-rendering module), i.e. $\mathbf{s}(t) = [\mathbf{s}_1(t) \ ... \ \mathbf{s}_k(t)]$ where $\mathbf{s}_k(t) = [\mathbf{k}_k \ \mathbf{c}_k^1 ... \mathbf{c}_k^{C+1}](t)$. In the lines of (Baradel et al., 2020), given the original initial condition and outcome $\mathbf{AB}$, CoDy estimates an unsupervised representation $\mathbf{u}_k$ of the latent confounder variables per keypoint k through the counterfactual estimator (*CF estimator* in Fig. 4). It first contextualizes the sequence $\mathbf{s}^{\mathbf{AB}}(t)$ through a graph network $\mathcal{GN}\big(\mathbf{s}^{\mathbf{AB}}(t)\big) = \mathbf{h}^{\mathbf{AB}}(t) = [\mathbf{h}_1(t) \ ... \ \mathbf{h}_K(t)]$. We then model the temporal evolution of this representation with a gated recurrent unit (Cho et al., 2014) per keypoint, sharing parameters over keypoints, taking as input the sequence $\mathbf{h}_k$. Its last hidden vector is taken as the confounder estimate $\mathbf{u}_k$.

Recent works on the Koopman Operator (Lusch et al., 2018) and Kazantzis-Kravaris-Luenberger Observer (Janny et al., 2021; Peralez & Nadri, 2021) have theoretically shown that, under mild assumptions, there exists a latent space of higher dimension, where a dynamical system given as an EDP can have a simpler dynamics. Inspired by this idea, we used an encoder-decoder structure within CoDy, which projects our dynamic system into a higher-dimensional state space, performs forecasting of the dynamics in this latent space, and then projects predictions back to the original keypoint space. Note that this dynamics encoder/decoder is different from the encoder/decoder of the de-rendering/rendering modules discussed in section 4.1. The state encoder $\mathcal{E}(\mathbf{s}(t)) = \boldsymbol{\sigma}(t)$ is modeled as a graph network $\mathcal{GN}$, whose aggregation function projects into an output embedding space $\boldsymbol{\sigma}(t)$ of dimension 256. The decoder $\Delta(\boldsymbol{\sigma}(t)) = \mathbf{s}(t)$ temporally processes the individual contextualized states $\boldsymbol{\sigma}(t)$ with a GRU, followed by new contextualization with a graph network $\mathcal{GN}$. Details on the full architecture are provided in appendix D.2.

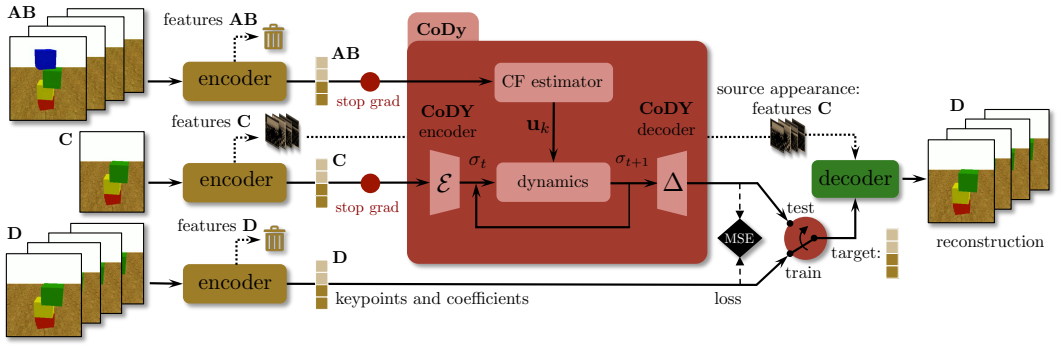

Figure 4: During training, we disconnect the dynamic prediction module (CoDy) from the rendering module (decoder). On test time, we reconnect the two modules. CoDy forecasts the counterfactual outcome $\mathbf{D}$ from the sparse keypoints representation of $\mathbf{AB}$ and $\mathbf{C}$. The confounders are discovered in an unsupervised manner and provided to the dynamical model.

The dynamic model CoDy performs forecasting in the higher-dimensional space $\boldsymbol{\sigma}(t)$, computing a displacement vector $\boldsymbol{\delta}(t+1)$ such that $\boldsymbol{\sigma}(t+1) = \boldsymbol{\sigma}(t) + \boldsymbol{\delta}(t+1)$. It takes the projected state embeddings $\sigma_k^{\mathbf{CD}}(t)$ per keypoint k concatenated with the confounder representation $\mathbf{u}_k$ and contextualizes them with a graph network, resulting in embeddings $\mathbf{h}_k^{\mathbf{CD}}(t) = \mathcal{GN}([\boldsymbol{\sigma}_{\boldsymbol{k}}^{\mathbf{CD}}(t), \mathbf{u}_k])$, which are processed temporally by a GRU. We compute the displacement vector at time $t+1$ as a linear transformation from the hidden state of the GRU. We apply the dynamic model in an auto-regressive way to forecast long-term trajectories in the projected space σ_k, and apply the state decoder to obtain a prediction $\hat{\mathbf{s}}^{\mathbf{CD}}(t)$.

The dynamic model is trained with a loss in keypoint space,

$$\mathcal{L}_{\text{physics}} = \sum_t \|\mathbf{s}^{\mathbf{CD}}(t) - \hat{\mathbf{s}}^{\mathbf{CD}}(t)\|_2^2 + \gamma_3 \|\mathbf{s}^{\mathbf{CD}}(t) - \Delta(\mathcal{E}(\mathbf{s}^{\mathbf{CD}}(t)))\|_2^2. \tag{6}$$

The first term enforces the model to learn to predict the outcomes and the second term favors correct reconstruction of the state in keypoint space. The terms are weighted with a scalar parameter γ_3.

4.3 Training

End-to-end training of all three modules jointly is challenging, as the same pipeline controls both the keypoint-based state representation and the dynamic module (CoDy), involving two adversarial objectives: optimizing reconstruction pushes the keypoint encoding to be as representative as possible, but learning the dynamics favors a simple representation. Faced with these two contradictory tasks, the model is numerically unstable and rapidly converges to regression to the mean. As described above, we separately train the encoder+decoder pair without dynamic information on reconstruction only, c.f. Equation (4). Then we freeze the parameters of the keypoint detector and train CoDy to forecast the keypoints from $\mathbf{D}$ minimizing the loss in Equation (6).

5 Experiments

We compare the proposed model to two strong baselines for physics-inspired video prediction.

- **PhyDNet** (Le Guen & Thome, 2020) is a non-counterfactual video prediction model that forecasts future frames using a decomposition between (a) a feature vector that temporally evolves via an LSTM and (b) a dynamic state that follows a PDE learned through specifically designed cells.
- **V-CDN** (Li et al., 2020) is a counterfactual model based on keypoints, close to our work. It identifies confounders from the beginning of a sequence and learns a keypoint predictor through auto-encoding using the Transporter equation (see discussion in Sect. 4.1). As it is, it cannot be used for video prediction and is incomparable with our work, see details in appendix C. We therefore replace the Transporter by our own de-rendering/rendering modules, from which we remove the additional coefficients. We refer to this model as UV-CDN (for Unsupervised V-CDN).

		Ours N	**Ours** 2N	UV-CDN N	UV-CDN 2N	PhyDNET
BlockTowerCF	PSNR	23.48	**24.69**	21.07	21.99	16.49
	L-PSNR	21.75	**23.03**	19.68	20.43	14.05
BallsCF	PSNR	21.19	**21.33**	19.51	19.54	18.56
	L-PSNR	**27.88**	27.16	25.49	25.67	16.51
CollisonCF	PSNR	**24.09**	**24.09**	23.73	23.83	19.69
	L-PSNR	23.32	**23.46**	22.60	23.16	18.14

Table 1: Comparison with the state-of-the-art models in physics-inspired machine learning of video signals, reporting reconstruction error (PSNR and introduced L-PSNR).

	Copy B	Copy C	**Ours**
BlockTowerCF	43.2	20.0	**9.58**
BallsCF	44.3	92.3	**36.12**
CollisionCF	7.6	40.3	**5.14**

Copy B: assumes absence of intervention (always outputs sequence **B**).
Copy C: assumes that the tower is stable (always outputs input **C**).

Table 2: Comparison with copying baselines. We report MSE$\times 10^{-3}$ on prediction of keypoints + coefficients.

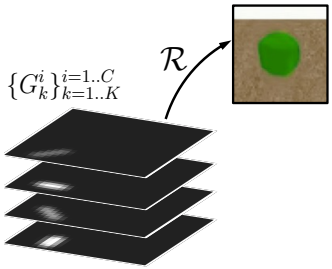

Figure 5: Network $\mathcal{R}$ learns a distortion from multiple oriented ellipses to target shapes.

# Coefficients:		✓			✗		
# Keypoints:		N	2N	4N	N	2N	4N
BlockTowerCF	PSNR	23.48	**24.69**	23.54	22.71	23.28	23.17
	L-PSNR	21.75	**23.03**	21.80	21.18	21.86	21.70
BallsCF	PSNR	21.19	21.33	**21.37**	20.49	21.09	20.97
	L-PSNR	**27.88**	27.16	27.07	26.33	27.07	26.73
CollisionCF	PSNR	24.09	24.09	**24.26**	23.84	23.66	24.06
	L-PSNR	23.32	**23.46**	23.44	22.58	22.81	23.45

Table 3: Impact of having additional orientation/shape coefficients (✓) compared to the keypoint-only solution (✗), for different numbers of keypoints: equal to number of objects ($= N$), $2N$ and $4N$.

All models have been implemented in PyTorch. The architectures of our modules are described in appendix D. For the baselines PhyDNet and UV-CDN, we used the official source code provided by the authors. We evaluate on each scenario of **Filtered-CoPhy** on the counterfactual video prediction task. For the two counterfactual models (Ours and UV-CDN), we evaluate on the tasks as intended: we provide the observed video sequence $\mathbf{AB}$ and the counterfactual initial condition $\mathbf{C}$, and forecast the sequence $\mathbf{D}$. PhyDNet, which is an inherently non-counterfactual model, requires an adaptation, which gives it information on the initial condition of the system to partially compensate for the absence of confounder estimates. We provide it with the first 10 frames of $\mathbf{CD}$, to allow the model to identify the initial velocity that cannot be inferred from a single image.

We measure performance with the standard time-averaged peak signal-to noise ratio (**PSNR**) that directly measures reconstruction quality. However, this metric is mainly dominated by error on the static background, which is not our main interest. We also introduce Localized PSNR (**L-PSNR**), which measures area on the important regions near moving objects. It corresponds to the PSNR on patches of 20×20 pixels centered on GT 2D positions of each object, averaged over patches.

Comparison to the SOTA — We compare our model against U-VCDN and PhyDNet in Table 1, consistently and significantly outperforming both baselines. The gap with UV-CDN is particularly interesting, as it confirms the choice of additional coefficients to model the dynamics of moving objects. Fig. 6 visualizes the prediction on a single example, more can be found in appendix E. We also compare to trivial copying baselines in Table 2, namely Copy B, which assumes no intervention and outputs the $\mathbf{B}$ sequence, and Copy C, which assumes a stable tower. We evaluate these models in keypoints space measuring MSE on keypoints and coefficients averaged over time, as copying baselines are unbeatable in the regions of static background, making the PSNR metrics unusable.

Impact of appearance coefficients — We report the impact of the additional coefficients in Table 3, comparing to the baseline using a keypoint-only latent representation. The coefficients have a significant impact: even increasing the number of keypoints to compensate for the loss of information in the latent representation cannot overcome the advantage of disentangling positions and shapes, as done in our model. We provide a deeper analysis of the de-rendering/rendering modules in appendix

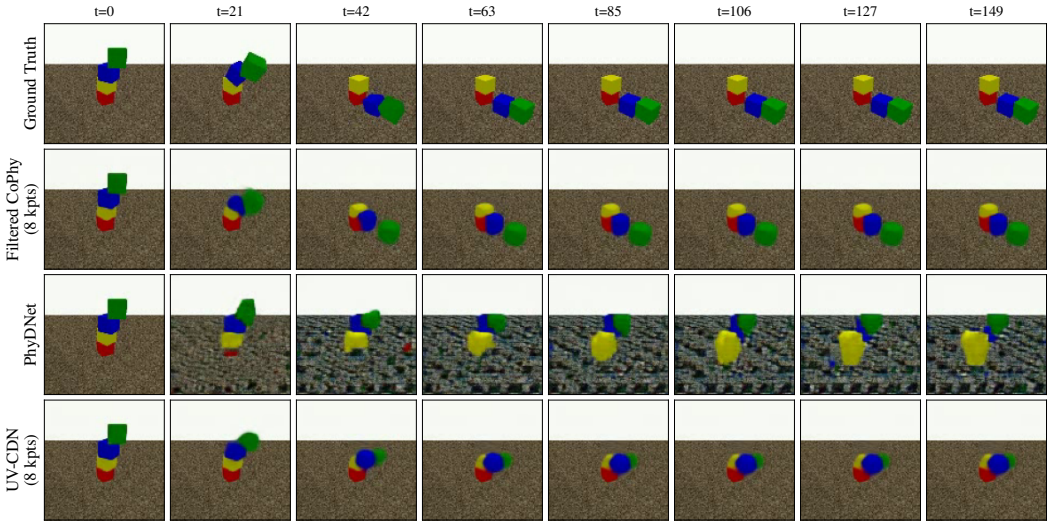

Figure 6: Visualization of the counterfactual video prediction quality, comparing our proposed model (Filtered CoPhy) with the two baselines, PhyDNet and UV-CDN, over different timestamps.

State auto-encoder:	✓	✗
BlocktowerCF	**9.58**	11.10
BallsCF	**36.12**	36.88
CollisionCF	**5.14**	16.16

Table 4: Impact of the dynamic CoDy encoder (✓) against the baseline operating in the keypoint + coefficient space (✗). We report MSE$\times 10^{-3}$ on prediction of keypoints + coefficients (4 pts).

Filter bank:	Fixed	Learned
BlocktowerCF	**34.40**	32.04
BallsCF	**37.76**	31.25
CollisionCF	**34.09**	33.88

Table 5: Learning the filter bank $\mathbf{H}$ from scratch has a mild negative effect on the reconstruction task. We report the PSNR on static reconstruction performance without the dynamic model.

B, which includes visualizations of the navigation of the latent shape space in B.2. We also compare the corresponding unsupervised objective with Transporter (Kulkarni et al., 2019) in appendix C.

Learning filters — does not have a positive impact on reconstruction performance compared to the choice of the handcrafted bank, as can be seen in table 5. We conjecture that the additional degrees of freedom are redundant with parts of the filter kernels in the refinement module $\mathcal{R}$: this corresponds to jointly learning a multi-channel representation $\{G_k^i\}_{k=1..K}^{i=1..C}$ for shapes as well as the mapping which geometrically distorts them into the target object shapes. Fixing the latent representation does not constrain the system, as the mapping $\mathcal{R}$ can adjust to it — see Fig. 5.

Impact of the high-dimensional dynamic space — We evaluate the impact of modeling object dynamics in high-dimensional space through the CoDy encoder in Table 4, comparing projection to 256 dimensions to the baseline reasoning directly in keypoint + coefficient space. The experiment confirms this choice of KKL-like encoder (Janny et al., 2021).

6 Conclusion

We introduced a new benchmark for counterfactual reasoning in physical processes requiring to perform video prediction, i.e. predicting raw pixel observations over a long horizon. The benchmark has been carefully designed and generated imposing constraints on identifiability and counterfactuality. We also propose a new method for counterfactual reasoning, which is based on a hybrid latent representation combining 2D keypoints and additional latent vectors encoding appearance and shape. We introduce an unsupervised learning algorithm for this representation, which does not require any supervision on confounders or other object properties and processes raw video.

REFERENCES

Alexander Balke and Judea Pearl. Counterfactual probabilities: Computational methods, bounds and applications. In *UAI*, 1994.

Fabien Baradel, Natalia Neverova, Julien Mille, Greg Mori, and Christian Wolf. Cophy: Counterfactual learning of physical dynamics. In *International Conference on Learning Representations*, 2020.

Peter Battaglia, Razvan Pascanu, Matthew Lai, Danilo Jimenez Rezende, and Koray kavukcuoglu. Interaction networks for learning about objects, relations and physics. In *Proceedings of the 30th International Conference on Neural Information Processing Systems*, 2016.

Kyunghyun Cho, Bart van Merriënboer, Caglar Gulcehre, Dzmitry Bahdanau, Fethi Bougares, Holger Schwenk, and Yoshua Bengio. Learning phrase representations using RNN encoder–decoder for statistical machine translation. In *Conference on Empirical Methods in Natural Language Processing*, 2014.

Emmanuel de Bezenac, Arthur Pajot, and Patrick Gallinari. Deep learning for physical processes: Incorporating prior scientific knowledge. In *International Conference on Learning Representations*, 2018.

Emily L. Denton and Vighnesh Birodkar. Unsupervised learning of disentangled representations from video. *ArXiv*, abs/1705.10915, 2017.

Chelsea Finn, Ian Goodfellow, and Sergey Levine. Unsupervised learning for physical interaction through video prediction. In *Proceedings of the 30th International Conference on Neural Information Processing Systems*, 2016.

Catalin Ionescu, Dragos Papava, Vlad Olaru, and Cristian Sminchisescu. Human3.6m: Large scale datasets and predictive methods for 3d human sensing in natural environments. *IEEE Transactions on Pattern Analysis and Machine Intelligence*, 2014.

Steeven Janny, Madiha Nadri Vincent Andrieu, and Christian Wolf. Deep kkl: Data-driven output prediction for non-linear systems. In *Conference on Decision and Control (CDC21)*, 2021.

Tejas D. Kulkarni, Ankush Gupta, Catalin Ionescu, Sebastian Borgeaud, Malcolm Reynolds, Andrew Zisserman, and Volodymyr Mnih. Unsupervised learning of object keypoints for perception and control. In *Advances in Neural Information Processing Systems 32: Annual Conference on Neural Information Processing Systems 2019*, 2019.

Y. Kwon and M. Park. Predicting future frames using retrospective cycle gan. *2019 IEEE/CVF Conference on Computer Vision and Pattern Recognition (CVPR)*, pp. 1811–1820, 2019.

Vincent Le Guen and Nicolas Thome. Disentangling physical dynamics from unknown factors for unsupervised video prediction. In *Computer Vision and Pattern Recognition (CVPR)*, 2020.

Yunzhu Li, Antonio Torralba, Anima Anandkumar, Dieter Fox, and Animesh Garg. Causal discovery in physical systems from videos. *Advances in Neural Information Processing Systems*, 33, 2020.

Francesco Locatello, Dirk Weissenborn, Thomas Unterthiner, Aravindh Mahendran, G. Heigold, Jakob Uszkoreit, A. Dosovitskiy, and Thomas Kipf. Object-centric learning with slot attention. *ArXiv*, abs/2006.15055, 2020.

David G. Lowe. Object recognition from local scale-invariant features. In *ICCV*, 1999.

Chaochao Lu, Michael Hirsch, and Bernhard Schölkopf. Flexible spatio-temporal networks for video prediction. In *2017 IEEE Conference on Computer Vision and Pattern Recognition (CVPR)*, 2017.

Bethany Lusch, Nathan Kutz, and Steven Brunton. Deep learning for universal linear embeddings of nonlinear dynamics. *Nature Communications*, 2018.

Lucas Manuelli, Wei Gao, Peter R. Florence, and Russ Tedrake. kpam: Keypoint affordances for category-level robotic manipulation. *ArXiv*, abs/1903.06684, 2019.

Lucas Manuelli, Yunzhu Li, Peter R. Florence, and Russ Tedrake. Keypoints into the future: Self-supervised correspondence in model-based reinforcement learning. *CoRR*, 2020.

G. Martin-Ordas, J. Call, and F. Colmenares. Tubes, tables and traps: great apes solve twofunctionally equivalent trap tasks but show no evidence of transfer across tasks. *Animal cognition*, 11(3): 432–430, 2008.

Michael Mathieu, Camille Couprie, and Yann LeCun. Deep multi-scale video prediction beyond mean square error. In *4th International Conference on Learning Representations, ICLR 2016, San Juan, Puerto Rico, May 2-4, 2016, Conference Track Proceedings*, 2016.

Matthias Minderer, Chen Sun, Ruben Villegas, Forrester Cole, K. Murphy, and Honglak Lee. Unsupervised learning of object structure and dynamics from videos. *ArXiv*, abs/1906.07889, 2019.

Judea Pearl. *Causality: Models, Reasoning and Inference*. Cambridge University Press, 2000.

Judea Pearl. Causal and counterfactual inference. *The Handbook of Rationality*, pp. 1–41, 2018.

Johan Peralez and Madiha Nadri. Deep learning-based luenberger observer design for discrete-time non-linear systems. In *Conference on Decision and Control (CDC21)*, 2021.

Bernhard Schölkopf, Francesco Locatello, Stefan Bauer, Nan Rosemary Ke, Nal Kalchbrenner, Anirudh Goyal, and Yoshua Bengio. Toward causal representation learning. *Proceedings of the IEEE*, 2021.

Nitish Srivastava, Elman Mansimov, and Ruslan Salakhutdinov. Unsupervised learning of video representations using lstms. In *Proceedings of the 32nd International Conference on International Conference on Machine Learning - Volume 37*, 2015.

Supasorn Suwajanakorn, Noah Snavely, Jonathan Tompson, and Mohammad Norouzi. Discovery of latent 3d keypoints via end-to-end geometric reasoning. In *NeurIPS 2018*, 2018.

Rishi Veerapaneni, John D. Co-Reyes, Michael Chang, Michael Janner, Chelsea Finn, Jiajun Wu, Joshua Tenenbaum, and Sergey Levine. Entity abstraction in visual model-based reinforcement learning. In *Proceedings of the Conference on Robot Learning*, 2020.

Ruben Villegas, Jimei Yang, Seunghoon Hong, Xunyu Lin, and Honglak Lee. Decomposing motion and content for natural video sequence prediction. In *ArXiv*, volume abs/1706.08033, 2017a.

Ruben Villegas, Jimei Yang, Yuliang Zou, Sungryull Sohn, Xunyu Lin, and Honglak Lee. Learning to generate long-term future via hierarchical prediction. In *ICML*, 2017b.

Carl Vondrick, Hamed Pirsiavash, and Antonio Torralba. Generating videos with scene dynamics. In *Proceedings of the 30th International Conference on Neural Information Processing Systems*, 2016.

Jacob Walker, Kenneth Marino, Abhinav Gupta, and M. Hebert. The pose knows: Video forecasting by generating pose futures. *2017 IEEE International Conference on Computer Vision (ICCV)*, pp. 3352–3361, 2017.

Kexin Yi, Chuang Gan, Yunzhu Li, Pushmeet Kohli, Jiajun Wu, Antonio Torralba, and Joshua B. Tenenbaum. CLEVRER: collision events for video representation and reasoning. In *ICLR*, 2020.

Yuan Yin, Vincent LE GUEN, Jérémie DONA, Emmanuel de Bezenac, Ibrahim Ayed, Nicolas THOME, and patrick gallinari. Augmenting Physical Models with Deep Networks for Complex Dynamics Forecasting. In *International Conference on Learning Representations (ICLR)*, 2021.

Appendix

A FURTHER DETAILS ON DATASET GENERATION

Confounders — are masses, which we discretize in $\{1, 10\}$. For `BallsCF` and `CollisionCF`, we can also consider the (continuous) initial velocities of each object as confounders variables, since they have to be identified in $\mathbf{AB}$ to forecast $\mathbf{CD}$.

We simulate all the trajectories associated with the various possible combinations of masses from the same initial condition.

Do-interventions — depend on the task. For `BlocktowerCF` and `BallsCF`, do-interventions consist in (a) removing the top cube or a ball, or (b) shifting a cube/ball on the horizontal plane. In this case, for `BlocktowerCF`, we make sure that the cube does not move too far from the tower, in order to maintain contact. For `CollisionCF`, the do-interventions are restricted to shifting operations, since there are only two objects (a ball and a cylinder). It can consist of either a flip of the cylinder orientation between vertical or horizontal, or a shift of the position of the moving object relative to the resting one in one of the three canonical directions x, y and z.

A.1 ENFORCING THE IDENTIFIABILTY CONSTRAINT

The identifiabilty and counterfactuality constraints described in section 3 are imposed numerically, i.e. we simulated trajectories and reject trajectories which violate constraints.

As stated in section 3, an identifiable experiment guarantees that there is no pair (z, z') that gives the same trajectory $\mathbf{AB}$ but a different counterfactual outcome $\mathbf{CD}$. Otherwise, there will be no way to choose between z and z' only from looking at $\mathbf{AB}$, thus no way to correctly forecast the counterfactual experiment. By enforcing this constraint, we make sure that there exists at least a set $\{z, z', ...\}$ of confounders that gives at the same time similar observed outcomes $\mathbf{AB}$ and similar counterfactual outcomes $\mathbf{CD}$.

In practice, there exists a finite set of possible variables z_i, corresponding to every combination of masses for each object in the scene (masses take their value in $\{1, 10\}$). During generation, we submit each candidate experiment $(\mathbf{AB}, \mathbf{CD}, z)$ to a test ensuring that the candidate is identifiable. Let $\psi(X_0, z)$ be the function that gives the trajectory of a system having for initial condition X_0 and for confounders z. We simulate all the possible trajectories $\psi(A, z_i)$ and $\psi(C, z_i)$ for every possible z_i. If there exists $z' \neq z$ such that the experiment is not identifiable, the candidate is rejected. This constraint requires to simulate the trajectory of each experiment several times by modifying the physical properties of the objects.

Equalities in Definition 1 are relaxed by thresholding distances between trajectories. We reject the candidate experiment if there exists a z' such that

$$\sum_{t=0}^{T} \|\psi(A, z) - \psi(A, z')\|_2 < \epsilon \text{ and } \sum_{t=0}^{T} \|\psi(C, z) - \psi(C, z')\|_2 > \epsilon. \tag{7}$$

The choice of the threshold value ϵ is a critical parameter, in particular for the identifiability constraint:

- If the threshold is **too high**, all $\mathbf{AB}$ trajectories will be considered as equal, which results in the acceptance of unidentifiable experiments.
- If the threshold is **too low**, all trajectories $\mathbf{CD}$ are considered equal. Again, this leads to mistakenly accepting unidentifiable experiments.

There exists an optimal value for ϵ, which allows to correctly reject unidentifiable experiences. To measure this optimal threshold, we generated a small instance of the `BlocktowerCF` dataset without constraining the experiments, i.e. trajectories can be unidentifiable and non counterfactual. We then plot the percentage of rejected experiments in this unfiltered dataset against the threshold

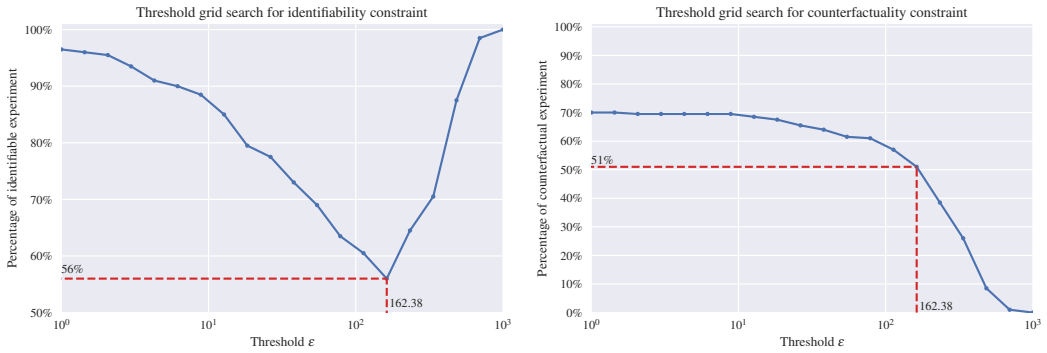

Figure 7: Experimental tuning of the threshold parameter. We generate an unconstrained subset of `BlocktowerCF` and plot the percentage of identifiable experiment in function of the threshold ϵ.

	without constraint	with constraint
Accuracy	56%	**84%**
Corrected Acc.	58%	**91%**

(a)

FPS	5	15	25	35	45
MSE ($\times 10^{-2}$)	4.58	3.97	**3.74**	3.82	3.93

(b)

Table 6: (a) Sanity check of the identifiability constraint in `BlocktowerCF`. The addition of the constraint allows better retrieval of the masses of each cubes. The corrected accuracy only consider determinants cube for forecasting $\mathbf{D}$. (b) MSE between ground truth 3D position and predicted position after 1 second, depending on the sampling rate of the trajectory.

value (Fig. 7, left). We chose the threshold $\epsilon = 100$ which optimizes discrimination and rejects the highest number of "unidentifiable" trajectories.

To demonstrate the interest of this improvement, we train a recurrent graph network on `BlocktowerCF` to predict the masses of the cubes from ground truth state trajectories $\mathbf{AB}$, including pose and velocities, see Fig. 8. It outputs the masses of each cube as a binary classification task. We train this model on both `BlocktowerCF` and an alternative version of the scenario generated without the identifiability constraint, the results are shown in Table 6a. We are not aiming 100% accuracy, and this problem remains difficult in a sense that the identifiability constraint ensures the identifiability of a set of confounder variables, while our sanity check tries to predict a unique z.

However, the addition of the identifiability constraint to the benchmark significantly improves the accuracy of the model, which indicates that the property acts positively on the the feasability of **Filtered-CoPhy**. The *corrected accuracy* metric focuses solely on the determining cubes for $\mathbf{CD}$, that is the cubes whose knowledge of their mass is essential to accurately predict the counterfactual outcome.

A.2 Enforcing the Counterfactuality constraint

Let $(\mathbf{AB}, \mathbf{CD}, z)$ be the candidate experiment, and z^k the combination of mass identical to z but whose k^{th} mass has been replaced. The constraint consists in checking that there exists at least one k such that $\psi(C, z) \neq \psi(C, z^k)$. To do so, we simulate $\psi(C, z^k)$ for all k, and we measure the difference with the candidate trajectory $\psi(C, z)$. Formally, we verify the existence of k such that:

$$\sum_{t=0}^{T} \|\psi(C, z^k) - \psi(C, z)\|_2 < \epsilon. \tag{8}$$

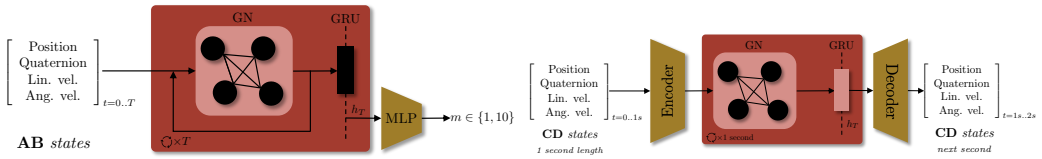

Figure 8: Impact of the choice of temporal resolution. Left: We check the identifiability constraint by training a model to predict the masses of the cubes in `BlocktowerCF` from the observed trajectory **AB**. The model is a graph neural network followed by a gated recurrent unit. Right: We check the augmentation of the sample rate by training an agent to forecast a 1 second-length trajectory from the states of the previous second.

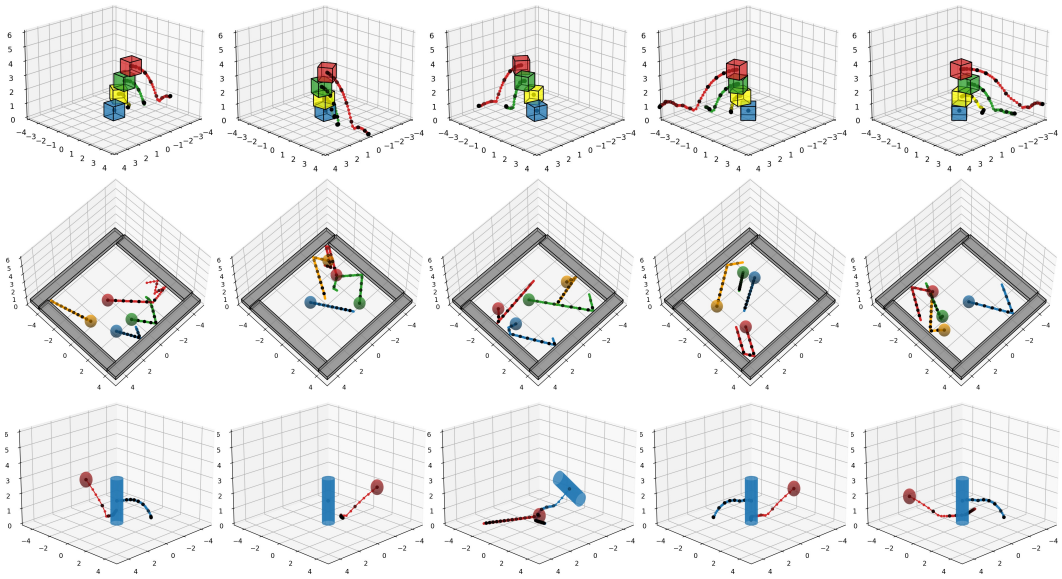

Figure 9: Visual examples of the impact of temporal resolution on dynamical information for each task in **Filtered-CoPhy**. Black dots are sampled at 6 FPS while red dots are sampled at 25 FPS.

A.3 Analyzing temporal resolution

We analyzed the choice of temporal frequency for the benchmark with another sanity check. We simulate a non counterfactual dataset from `BlocktowerCF` where all cubes have equal mass. A a recurrent graph network takes as input the cube trajectories (poses and velocities) over a time interval of one second and predicts the rest of the trajectory over the following second. We vary the sampling frequency; for example, at 5 FPS, the model receives 5 measurements, and predicts the next 5 time steps, which correspond to a one second rollout in the future. Finally, we compare the error in 3D position between the prediction and the GT on the last prediction (ie. the prediction error after 1 second of rollout). Results are shown in Table 6b. This check shows clearly that 25 FPS corresponds to a perfect trade-off between an accurate representation of the collision and the amount of training data. Fig. 9 shows a practical example of the effect of time resolution on dynamical information in a trajectory.

A.4 Simulation details

We used Pybullet as physics engine to simulate **Filtered-CoPhy**. Each experiment in the dataset has been generated in order to respect a balance a complete coverage of confounder combinations and counterfactuality and identifiability constraints described above. We generate the trajectories iteratively:

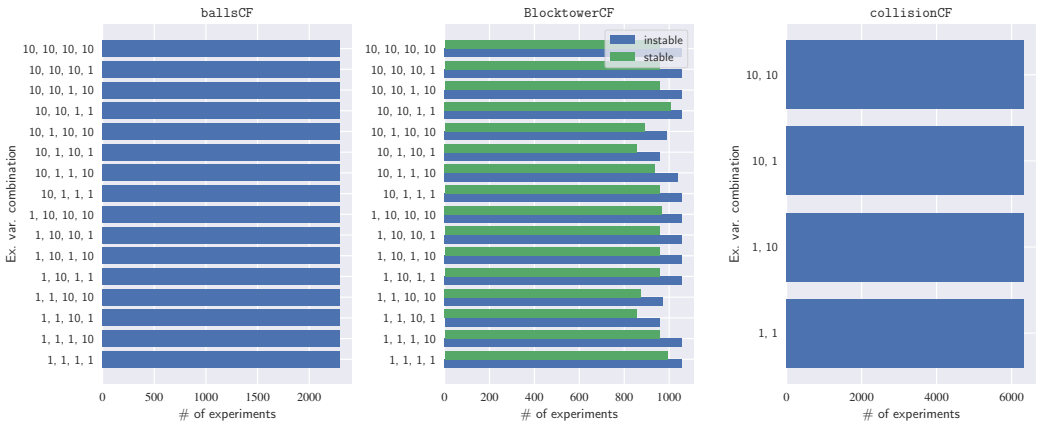

Figure 10: During the dataset generation process, we took care of keeping balance between the combinations of masses, i.e. the confounders. For `BlocktowerCF`, we also guarantees that the proportion of stable **CD** tower is close to 50% for each confounder configuration.

1. We sample a combination of masses and other physical characteristics of the given experiment, such as stability of the tower, or object motion in `CollisionCF`, or if the do-operation consists in removing an object. This allow us to maintain a balance of confounder configurations.
2. Then we search for an initial configuration $\mathbf{A}$. For `BlocktowerCF`, we make sure that this configuration is unstable to ensure identifiability. Then we simulate the trajectory $\mathbf{B}$.
3. We look for a valid do-operation such that identifiability and counterfactuality constraints are satisfied. If no valid do-operation is found after a fixed number of trials, we reject this experiment.
4. If a valid pair $(\mathbf{AB}, \mathbf{CD})$ is found, we save the experiment start a new one.

The trajectories were simulated with a sample time of 0.04 seconds. The video resolution is 448×448 and represents 6 seconds for `BlocktowerCF` and `BallsCF`, and 3 seconds for `CollisionCF`. We invite interested readers to look at our code for more precise details, such as do-operation sampling, or intrinsic camera parameters. Fig. 10 shows the confounder distribution in the three tasks.

B Performance evaluation of the de-rendering module

B.1 Image reconstruction

We evaluate the reconstruction performance of the de-rendering module and the reconstruction task. Note that there is trade-off between the reconstruction performance and dynamic forecasting accuracy: a higher number of keypoints may lead to better reconstruction, but can hurt prediction preformance, as the dynamic model is more difficult to learn.

# Keypoints		N	2N	4N
BlocktowerCF	*PSNR*	34.40	**35.41**	34.92
	MSE Grad	27.24	**21.39**	23.99
BallsCF	*PSNR*	**37.76**	37.06	36.98
	MSE Grad	**3.47**	3.77	3.95
CollisionCF	*PSNR*	32.00	**35.41**	34.42
	MSE Grad	32.00	**12.57**	17.09

Table 7: PSNR (dB) on the task of reconstructing target from the source (both randomly sampled from **Filtered-CoPhy**), using 5 coefficients per keypoint. We vary the number of keypoints in our model. N is the maximum number of object in the scene.

Reconstruction error – We first investigate the impact of the number of keypoints in Table 7 by measuring the Peak Signal to Noise Ratio (PSNR) between the target image and its reconstruction. We vary the number of keypoints among multiples of N, the maximum number of objects in the scene. Increasing the number of keypoints increases reconstruction quality (PSNR) up to certain point, but this advantage has to be potentially outweighted against a possible loss in dynamical prediction quality of. Furthermore,

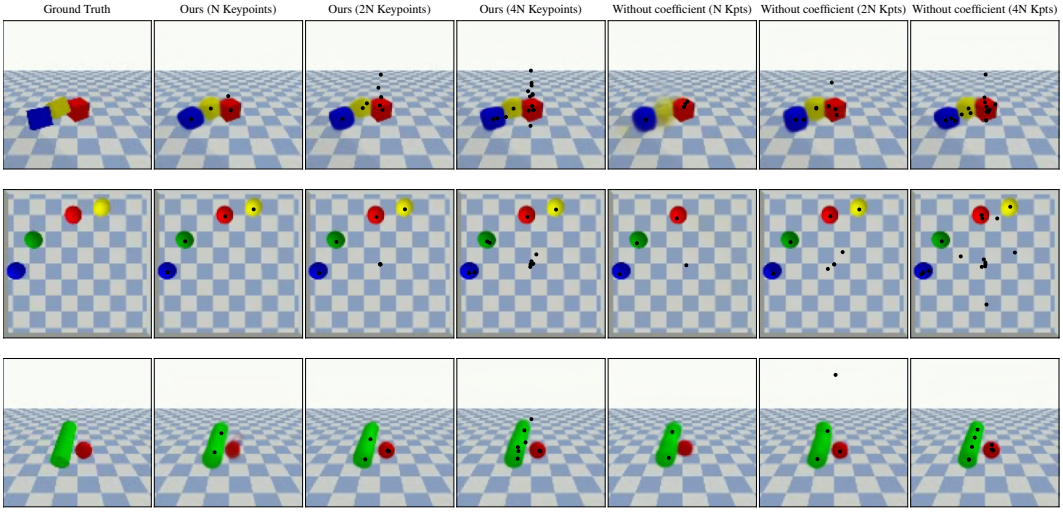

Figure 11: Reconstructions produced by the de-rendering module. Our model correctly marks each object in the scene and achieves satisfactory reconstruction.

doubling the number of keypoints only slightly improves reconstruction accuracy. This tends to indicate that our additional coefficients sufficiently manage to model visual details, which otherwise would have required several a larger number of keypoints for sufficient reconstruction. Table 3 in the main paper measures the impact of the number of keypoints and the presence or not of the additional appearance coefficients on the full pipeline including the dynamic model. To remove the effect on the representation on the dynamic model and to concentrate on reconstruction quality only, we perform an additional experiment, given in Table 8. As we can see, the addition of the coefficient consistently improves PSNR for low numbers of keypoints (over 2 decibel of progress for N keypoints). The improvement is less visible for larger numbers of keypoints, since 3D visual details could be encoded via keypoints position, hence coefficients become less relevant. Visualizations are shown in Fig. 11.

Coefficients		N		2N		4N	
		✗	✓	✗	✓	✗	✓
BlocktowerCF	*PSNR*	32.53	**34.40**	33.97	**35.41**	34.57	**34.92**
	MSE Grad	41.86	**27.24**	35.24	**21.39**	28.06	**23.99**
BallsCF	*PSNR*	34.62	**37.76**	36.94	**37.06**	**37.15**	36.98
	MSE Grad	6.22	**3.47**	4.16	**3.77**	**4.07**	3.95
CollisionCF	*PSNR*	30.65	**32.00**	33.89	**35.41**	**35.63**	34.42
	MSE Grad	12.78	**32.00**	20.59	**12.57**	**11.72**	17.09

Table 8: Impact of the number of keypoints and the presence of additional appearance coefficient in the de-rendering module for pure image reconstruction — no dynamic model was used in this experiment. We report PSNR (dB) and MSE on the image gradient. N is the maximum number of object in the scene. The coefficients significantly improve the reconstruction on low number of keypoints. This table is related to table 3 in the main part of the paper, which measures this impact on the full pipeline.

B.2 Navigating the latent coefficient manifold

We evaluate the influence of the additional appearance coefficients on our de-rendering model by navigating its manifold. To do so, we sample a random pair $(X_{\text{source}}, X_{\text{target}})$ from an experiment in `BlocktowerCF` and compute the corresponding source features and target keypoints and coefficients. Then, we vary each component of the target keypoints and coefficients and observe the reconstructed image. For ease of observation, we numerically remove every cube but one by setting

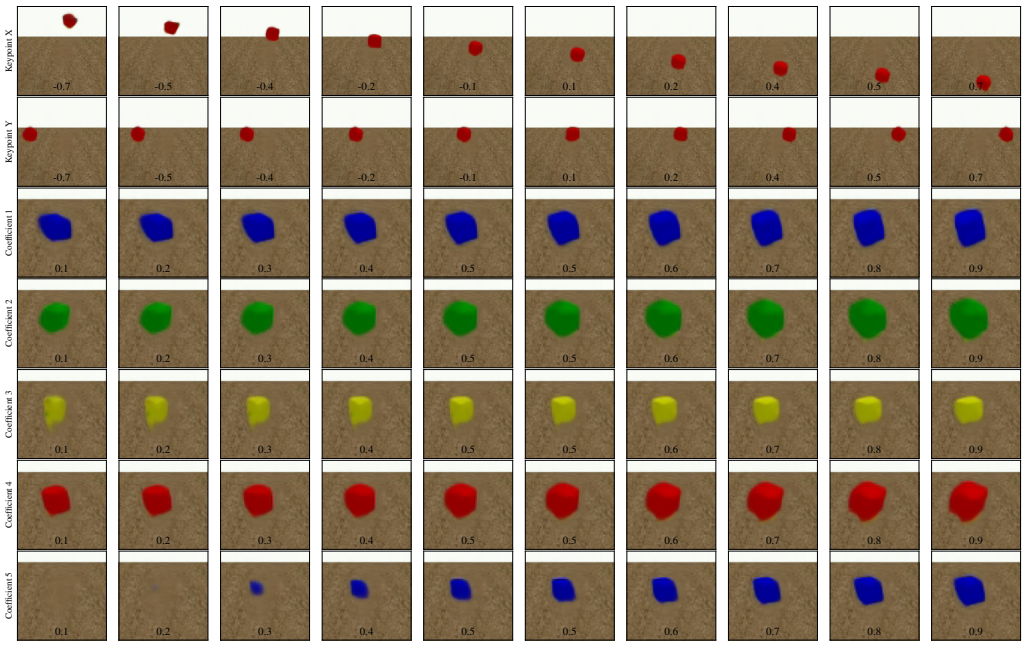

Figure 12: Navigating the manifold of the latent coefficient representation. Each line corresponds to variations of one keypoint coordinate or coefficient and shows the effect on a single cube.

their last coefficient to zero. Results are shown in fig. 12. We observed that the keypoints accurately control the position of the cube on both axis. The rendering module does infer some hints on 3D shape information from the altitude of the cube, exploiting a shortcut in learning. On other hand, while not being supervised, the coefficients naturally learn to encode different orientations in space, as well depth. Interestingly, some sort of disentanglement emerges from it. For example, coefficients n° 1 and 2 control some sort of rotation around the z-axis, and coefficient $n°4$ models rotation around the y-axis. The last coefficient represents, both, the size of the cube and its presence in the image.

C Comparison with the Transporter baseline

C.1 Comparison with our de-rendering model

As described in section 4.1, the Transporter (Kulkarni et al., 2019) is a keypoint detection model somewhat close to our de-rendering module. It leverages the transport equation to compute a reconstruction vector:

$$\hat{\Psi}_{\text{target}} = F_{\text{source}} \times (1 - K_{\text{source}}) \times (1 - K_{\text{target}}) + F_{\text{target}} \times K_{\text{target}}. \tag{9}$$

This equation allows to transmit information from the input by two means: the 2D position of the keypoints (K_{target}) and the dense visual features of the target (F_{target}). In comparison, our de-rendering solely relies on the keypoints from the target image and does not require a dense vector to be computed on the target to reconstruct the target. This makes the Transporter incomparable with our de-rendering module. We nevertheless compare the performances of the two models in Table 13, and provide visual examples in Fig. 13. Even though the two models are not comparable, as the Transporter uses additional information, our model still outperforms the Transporter for small numbers of keypoints. Interestingly, for higher numbers of keypoints, the Transporter tends to discover keypoints far from the object. We investigate this behavior in the following section, and shows that this is actually a critical problem for learning causal reasoning on the discovered keypoints.

	Ours			*Transporter* (not comparable)		
# Keypoints	4	8	16	4	8	16
BlockTowerCF	34.40	35.41	34.92	*34.10*	*34.88*	*39.20*
BallsCF	37.76	37.06	36.98	*34.75*	*34.78*	*35.13*
CollisionCF	35.41	34.42	35.98	*32.66*	*33.39*	*34.47*

Table 9: PSNR (dB) on the task of reconstructing target from the source (both randomly sampled from **Filtered-CoPhy**), using 5 coefficients per keypoint. We vary the number of keypoints in both our model and the Transporter. Note that Transporter uses target features to reconstruct the image, hence it is not comparable with our model.

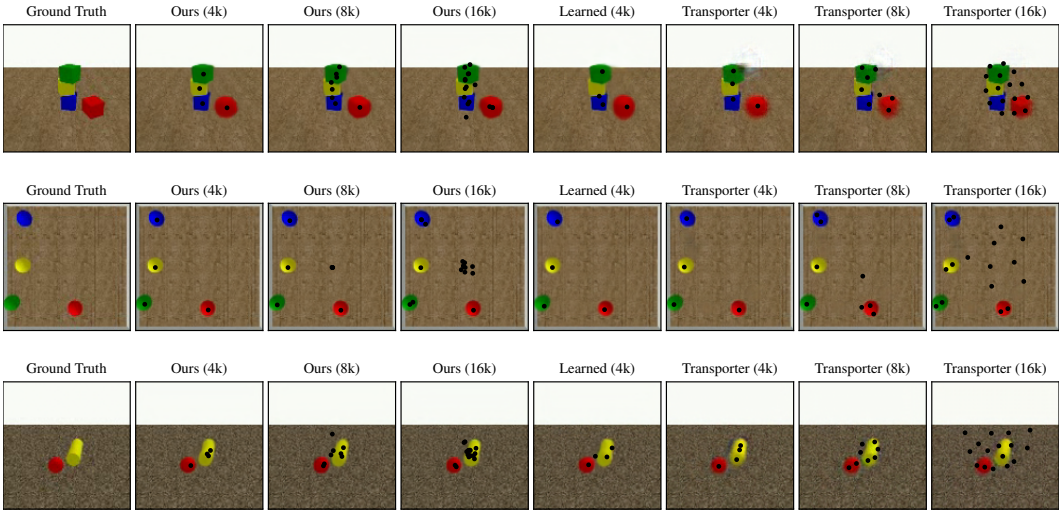

Figure 13: Example of reconstructed image by our-derendering module and the Transporter. Increasing the number of keypoints

C.2 Analysis of Transporter behavior

The original version of the V-CDN model (Li et al., 2020) is based on the Transporter (Kulkarni et al., 2019). We have already highlighted the fact that this model is not comparable with our task, as it requires not only the target keypoints K_{target} but also a dense feature map F_{target}, whose dynamics can hardly be learned due to its high-dimensionality. More precisely, the transport equation (Eq. 9) allows to pass information from the target by two means: the 2D position of the keypoints (K_{target}) and the dense feature map of the target (F_{target}). The number of keypoints therefore becomes a highly sensible parameter, as the transporter can decide to preferably transfer information through the target features rather than through the keypoint locations. When the number of keypoints is low, they act as a bottleneck, and the model has to carefully discover them to reconstruct the image. On other hand, when we increase the number of keypoints, the Transporter stops tracking objects in the scene and transfer visual information through the dense feature map, making the predicted keypoints unnecessary for image reconstruction, and therefore not representative of the dynamics.

To illustrate our hypothesis, we set up the following experiment. Starting from a trained Transporter model, we fixed the source image to be X_0 (the first frame from the trajectory) during the evaluation step. Then, we compute features and keypoints on the target frame X_t regularly sampled in time. We reconstruct the target image using the transport equation, *but without updating the target keypoints*. Practically, this consists in computing $\hat{\Psi}_{\text{target}}$ with Eq. (9) substituting K_{target} for K_{source}.

Results are shown in Fig. 14. There is no dynamical forecasting involved in this figure, and the Transporter we used was trained in a regular way, we only change the transport equation on evaluation time. We can notice that even though the keypoint positions have been fixed, the Transporter

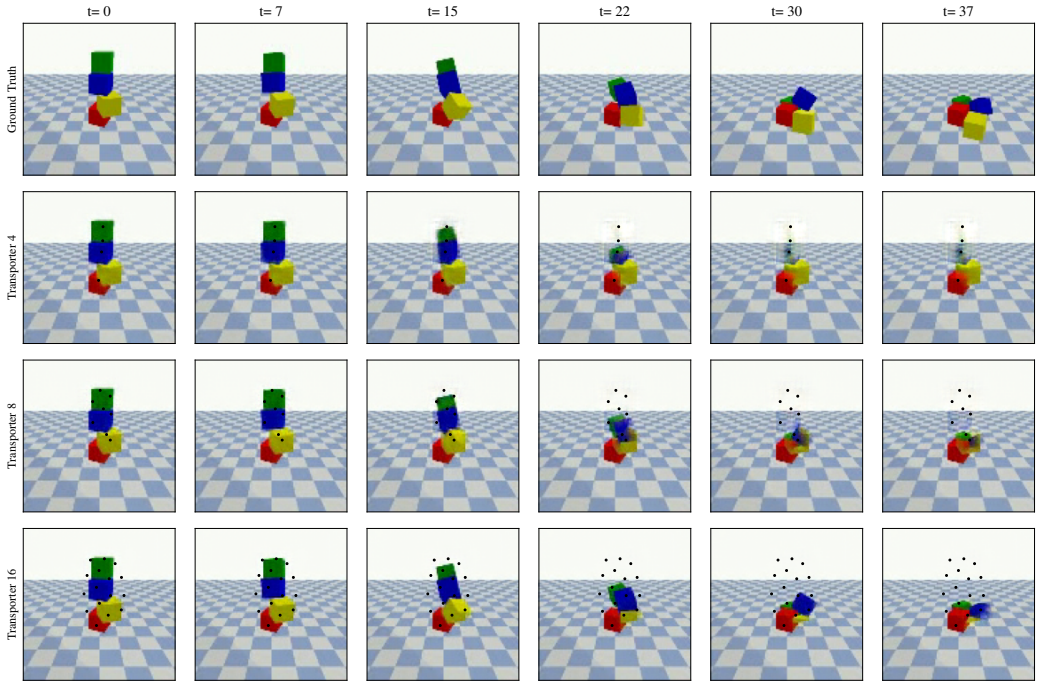

Figure 14: We evaluate the Transporter with varying number of keypoints to reconstruct images regularly sampled in a trajectory, but we fixed the target keypoints. Even if the keypoints are not moving, the Transporter still manages to reconstruct a significant part of the image, which indicates that the keypoints to do not well represent the dynamics of the scene.

manages to reconstruct a significant part of the images, which indicates that a part of the dynamics has been encoded in the dense feature map.

In contrast, this issue do not arise from our de-rendering module, since our decoder solely relies on the target keypoints to reconstruct the image. Note that this is absolutely not contradictory with the claim in Li et al. (2020), since they do not evaluate V-CDN in pixel space. A rational choice of the number of keypoints leads to satisfactory keypoints, allowing V-CDN to accurately forecast the trajectory in keypoints space, and retrieve the hidden confounders on their dataset.

C.3 Temporal consistency issues

Increasing the number of keypoints of the Transporter may lead to temporal consistency issues that arise in the long-range reconstruction task. For example, a keypoint that tracks the edge of a cube in the first frame may target a face of this same cube in the future, since dynamics does not intervene in the keypoint discovery process.

Our de-rendering directly addresses this through the usage of additional appearance coefficients, which allows to limit the number of keypoints to the number of objects in the scene, effectively alleviating the consistency issue. Fig. 15 illustrates this phenomenon by plotting the discovered keypoint locations forward in time, as well as the 2D location of the center of mass of each object. Note that the Transporter suffers from the temporal consistency issue with numbers of keypoints as low as 4 (green cube). In contrast, our model manages to solve the problem and accurately tracks the centers of mass, even though they were never supervised.

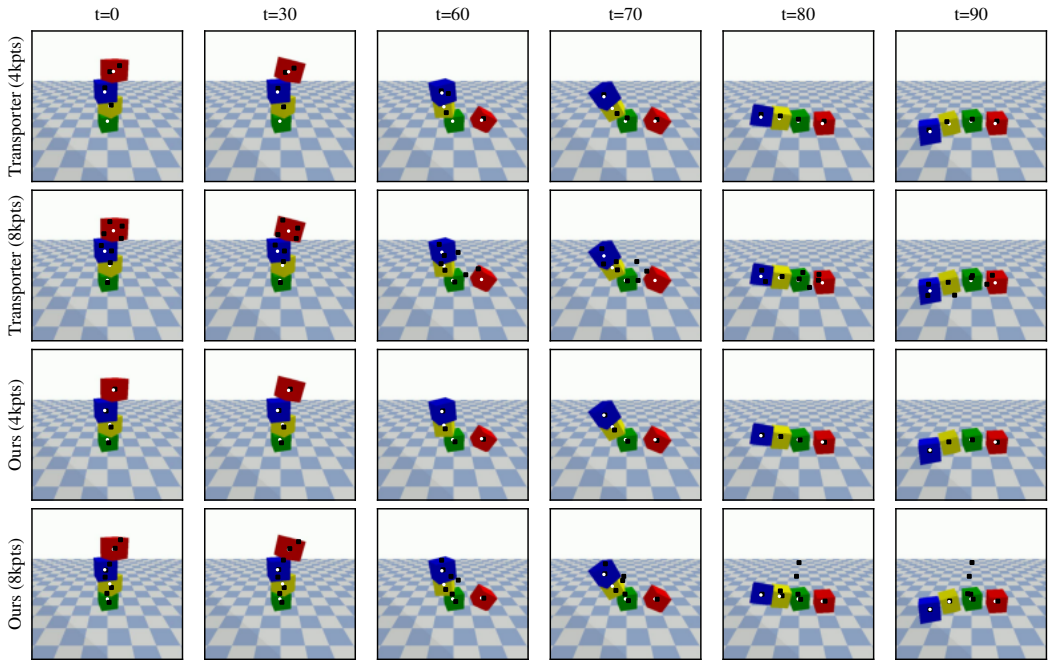

Figure 15: Illustration of the temporal consistency issue with long-range reconstruction. We show the keypoints discovered on images taken from different timesteps (black dots). We also compute the 2D location of the center of mass of each object in the scene (white dots). Our de-rendering module accurately tracks the centers of mass, which have never been supervised, which is a auspicious for learning object dynamics.

D DETAILS OF MODEL ARCHITECTURES

D.1 DERENDERING MODULE

In what follows, a "block" is a 2D convolutional layer followed by a 2D batch norm layer and ReLU activation. The exact architecture of each part of the encoder is described in Table 10a. The decoder hyper-parameters are described in Table 10b.

Dense feature map estimator $\mathcal{F}$ – We compute the feature vector from $\mathbf{X}_{\text{source}}$ by applying a convolutional network $\mathcal{F}$ on the output of the common CNN of the encoder. This produces the source features vector $\mathbf{F}_{\text{source}}$ of shape $(\text{batch}, 16, 28, 28)$.

Keypoin detector $\mathcal{K}$ – The convolutional network $\mathcal{K}$ outputs a set of 2D heatmaps of shape $(\text{batch}, K, 28, 28)$, where K is the desired number of keypoints. We apply a spatial softmax function on the two last dimensions, then we extract a pair of coordinate on each heatmap by looking for the location of the maximum, which gives us $\mathbf{K}_{\text{target}}$ of shape $(\text{batch}, K, 2)$.

Coefficient estimator $\mathcal{C}$ – We obtain the coefficient by applying a third convolutional network $\mathcal{C}$ to the output of the common encoder CNN, which again results in a set of 2D vectors of shape $(\text{batch}, K, 28, 28)$. These vectors are flattened channel wise and provide a tensor of shape $(\text{batch}, K, 28 \times 28))$ fed to an MLP (see Table 10a for the exact architecture) that estimates the coefficients $\mathbf{C}_{\text{target}}$ of shape $(\text{batch}, K, C+1)$.

Gaussian mapping $\mathcal{G}$ – The keypoint vector $\mathbf{K}_{\text{target}}$ is mapped to a 2D vector through a Gaussian mapping process :

$$\mathcal{G}(\mathbf{k})(x, y) = \exp\left(-\frac{(x-\mathbf{k}_x)^2 + (y-\mathbf{k}_y)^2}{\sigma^2}\right), \tag{10}$$

where $\mathcal{G}(\mathbf{k}) \in \mathbb{R}^{28\times 28}$ is the Gaussian mapping of the keypoint $\mathbf{k} = [\mathbf{k}_x \ \mathbf{k}_y]$. We deform these Gaussian mappings by applying convolutions with filters $\mathbf{H}_i$ controlled by the coefficients $\mathbf{c}_k^i$.

The filters from $\mathbf{H}$ are 5×5 dilatation kernels that elongate the Gaussian in a specific direction. Practically, we obtain the filter $\mathbf{H}_i$ by drawing a line crossing the center of the kernel and with a slope angle of $i\frac{\pi}{C}$ where C is the number of coefficients. We then apply a 2D convolution :

$$\mathbf{G}_k^i = \mathbf{c}_k^{C+1}\mathbf{c}_k^i \left(\mathcal{G}(\mathbf{k}_k) * \mathbf{H}_i\right). \tag{11}$$

Note that we also compute a supplementary coefficient α_k^{C+1} used as a gate on the keypoints. By setting this coefficient to zero, the de-rendering module can de-activate a keypoint (which is redundant with deactivating the full set of coefficients for this keypoint).

Refiner $\mathcal{R}$ **–** To reconstruct the target image, we channel-wise stack the feature vectors from the source with every deformed Gaussian mapping and feed them to the decoder CNN $\mathcal{R}$ (details in Table 10b).

We trained the de-rendering module on pairs of images $(\mathbf{X}_{\text{source}}, \mathbf{X}_{\text{target}})$ randomly sampled in $\mathbf{D}$ sequences of the experiments in the dataset. More precisely, for a given sequence $\mathbb{D}$, we sample the source image in the $T - 25$ first frames of the trajectory (where T is number of frame in the video). We sampled the target image 25 frames after the source. For evaluation, we sample the 25th frame to be the source image, and the 50th to be the target. We use the Adam algorithm with a learning rate set to 10^{-3} to minimize equation 4. We choose $\gamma_1 = 10^4$ and $\gamma_2 = 10^{-1}$.

CNN						
	Module	*in ch.*	*out ch.*	*kernel*	*stride*	*pad.*
1	Block	3	32	7	1	3
2		32	32	3	1	1
3		32	64	3	2	1
4		64	64	3	1	1
5		64	128	3	2	1

$\mathcal{F}()$						
1	Block	128	16	3	1	1

$\mathcal{K}()$						
1	Block	128	128	3	1	1
2	Conv2d	128	K	3	1	1
3	Softplus					

$\mathcal{C}()$						
1	Block	128	K	3	1	1
2	Flatten					
	Module	*in*	*out*			
3	Linear+ReLU	784	2048			
4	Linear+ReLU	2048	1024			
5	Linear+ReLU	1024	512			
6	Linear+ReLU	512	C			
7	Sigmoid					

(a) Encoder architecture

$\mathcal{R}()$						
		in ch.	*out ch.*	*kernel*	*stride*	*pad.*
1	Block	16+$K \times C$	128	3	1	1
2		128	128	3	1	1
3		128	64	3	1	1
4	UpSamplingBilinear2d(2)					
5	Block	64	64	3	1	1
6		64	32	3	1	1
7	UpSamplingBilinear2d(2)					
8	Block	32	32	3	1	1
9		32	32	7	1	1
10	Conv2d	32	3	1	1	1
11	TanH					

(b) Decoder architecture

Table 10: Architectural details of the de-rendering module.

D.2 CoDy

We describe the architectural choices made in CoDy. Let

$$\mathbf{s}(t) = [\mathbf{k}_k \; \mathbf{c}_k^1 \; ... \; \mathbf{c}_k^{C+1} \; \dot{\mathbf{k}}_k \; \dot{\mathbf{c}}_k^1 \; ... \; \dot{\mathbf{c}}_k^{C+1}]_{k=1..K} \tag{12}$$

be the state representation of an image $\mathbf{X}_t$, composed of the K keypoints 2D coordinates with their $C + 1$ coefficients. The time derivative of each component of the state is computed via an implicit

Euler derivation scheme $\dot{\mathbf{k}}(t) = \mathbf{k}(t) - \mathbf{k}(t-1)$. We use a subscript notation to distinguish the keypoints from $\mathbf{AB}$ and $\mathbf{CD}$.

CF estimator – The latent representation of the confounders is discovered from $\mathbf{s}^{\mathbf{AB}}$. The graph neural network from this module implements the message passing function $f()$ and the aggregation function $g()$ (see equation 5) by an MLP with 3 hidden layers of 64 neurons and ReLU activation unit. The resulting nodes embeddings $\mathbf{h}^{\mathbf{AB}}(t) = \mathcal{GN}(\mathbf{s}^{\mathbf{AB}}(t))$ belong to $\mathbb{R}^{128}$. We then apply a gated recurrent unit with 2 layers and a hidden vector of size 32 to each node in $\mathbf{h}^{\mathbf{AB}}(t)$ (sharing parameters between nodes). The last hidden vector is used as the latent representation of the confounders u_k.

State encoder-decoder – The state encoder is modeled as a $\mathcal{GN}$ where the message passing function and the aggregation function are MLPs with one hidden layer of 32 units. The encoded state $\boldsymbol{\sigma}^{\mathbf{CD}} = \mathcal{E}(s^{\mathbf{CD}})$ lies in $\mathbb{R}^{256}$. We perform dynamical prediction in this $\boldsymbol{\sigma}$ space, and then project back the forecasting in the keypoint space using a decoder. The decoder $\Delta(\boldsymbol{\sigma}(t))$ first applies a shared GRU with one layer and a hidden vector size of 256 to each keypoint $\boldsymbol{\sigma}_k(t)$, followed by a graph neural network with the same structure as the state encoder.

Dynamical system – Our dynamical system forecasts the future state $\hat{\boldsymbol{\sigma}}(t+1)$ from the current estimation $\hat{\boldsymbol{\sigma}}(t)$ and the confounders $\mathbf{u} = [\mathbf{u}_1 \ ... \ \mathbf{u}_K]$. It first applies a graph neural network to the concatenated vector $[\hat{\boldsymbol{\sigma}}(t) \ \mathbf{u}]$. The message passing function f and the aggregation function g are MLPs with 3 hidden layers of 64 neurons and ReLU activation function. The resulting nodes embeddings $\mathcal{GN}((\sigma)(t))$ belong to $\mathbb{R}^{64}$ and are fed to a GRU sharing weights among each nodes with 2 layers and a hidden vector of size 64. This GRU updates the hidden vector $\mathbf{v}^{\mathbf{CD}}(t) = [\mathbf{v}_1 \ ... \ \mathbf{v}_K]$, that is then used to compute a displacement vector with a linear transformation:

$$\hat{\boldsymbol{\sigma}}_k(t+1) = \boldsymbol{\sigma}_{\boldsymbol{k}}(t) + \mathbf{W}\mathbf{v}_{\mathbf{k}}(t) + \mathbf{b} \tag{13}$$

CoDy is trained via Adam SGD to minimize equation 6 with a learning rate set to 10^{-4} and $\gamma_3 = 1$. We train each CoDy instance by providing it the fixed keypoints states $\mathbf{s}^{\mathbf{AB}}(t)$ and the initial condition $\mathbf{s}^{\mathbf{CD}}(t=0)$ computed by our trained de-rendering module. CoDy first computes the latent confounder representation $\mathbf{u}_k$, and then projects the initial condition condition into the latent dynamical space $\boldsymbol{\sigma}(t=0) = \mathcal{E}(\mathbf{s}^{\mathbf{CD}}(t=0))$. We apply the dynamical multiple times in order to recursively forecast the T time-steps from $\mathbf{CD}$. We then apply the decoder $\Delta(\hat{\boldsymbol{\sigma}}(t))$ to compute the trajectory in the keypoint space.

E QUALITATIVE EVALUATION: MORE VISUAL EXAMPLES

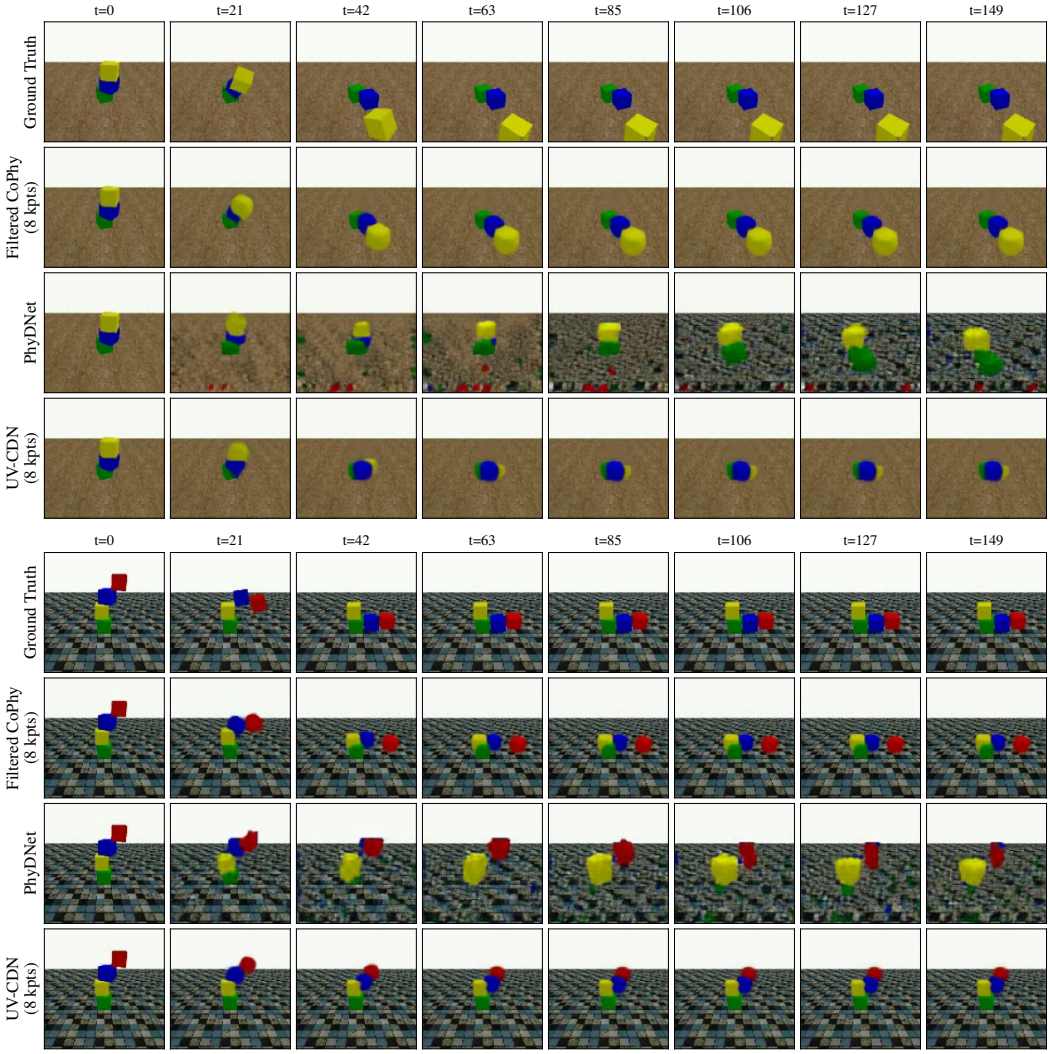

Figure 16: The CoPhy benchmark suite is subdivided in three scenarios involving 2D or 3D rigid body dynamics with complex interactions, including collision and resting contact.

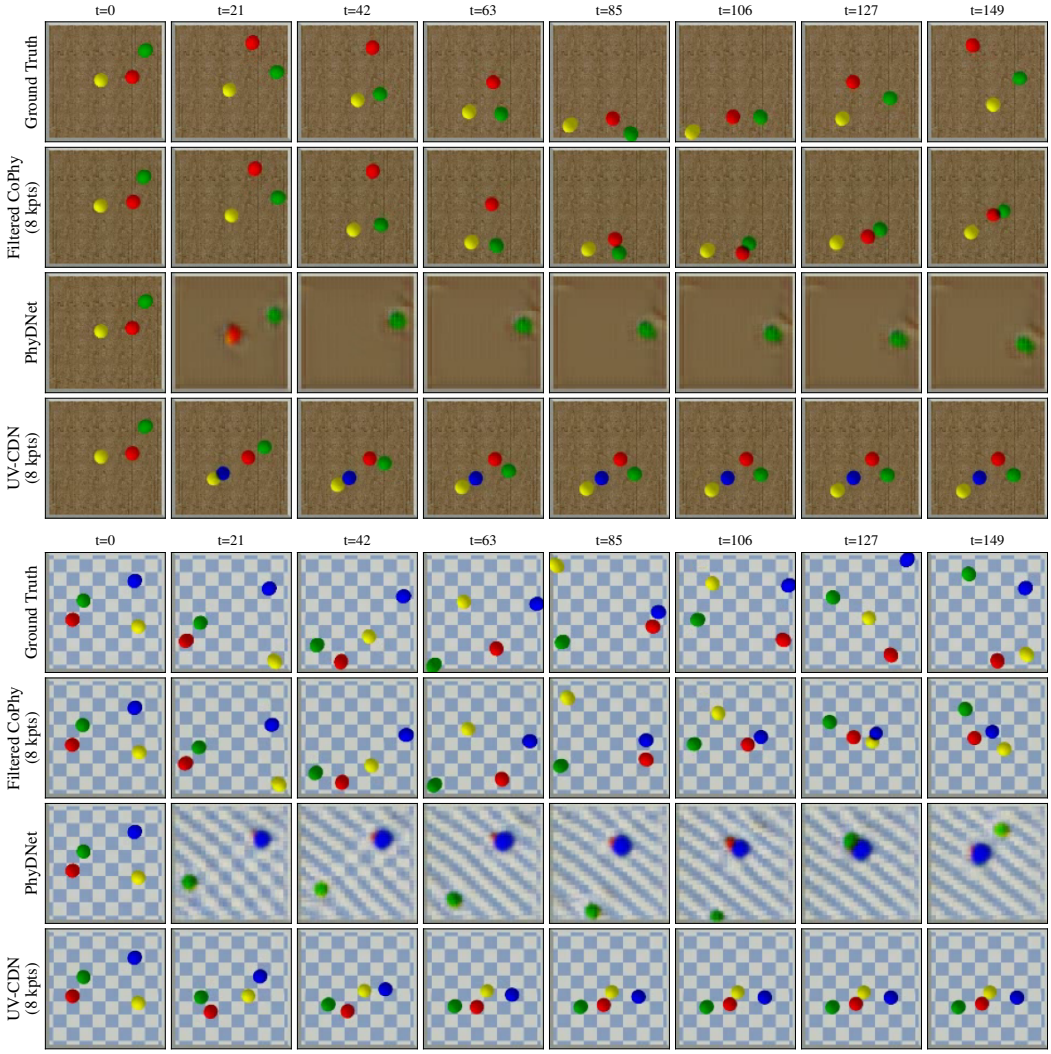

Figure 17: The CoPhy benchmark suite is subdivided in three scenarios involving 2D or 3D rigid body dynamics with complex interactions, including collision and resting contact.

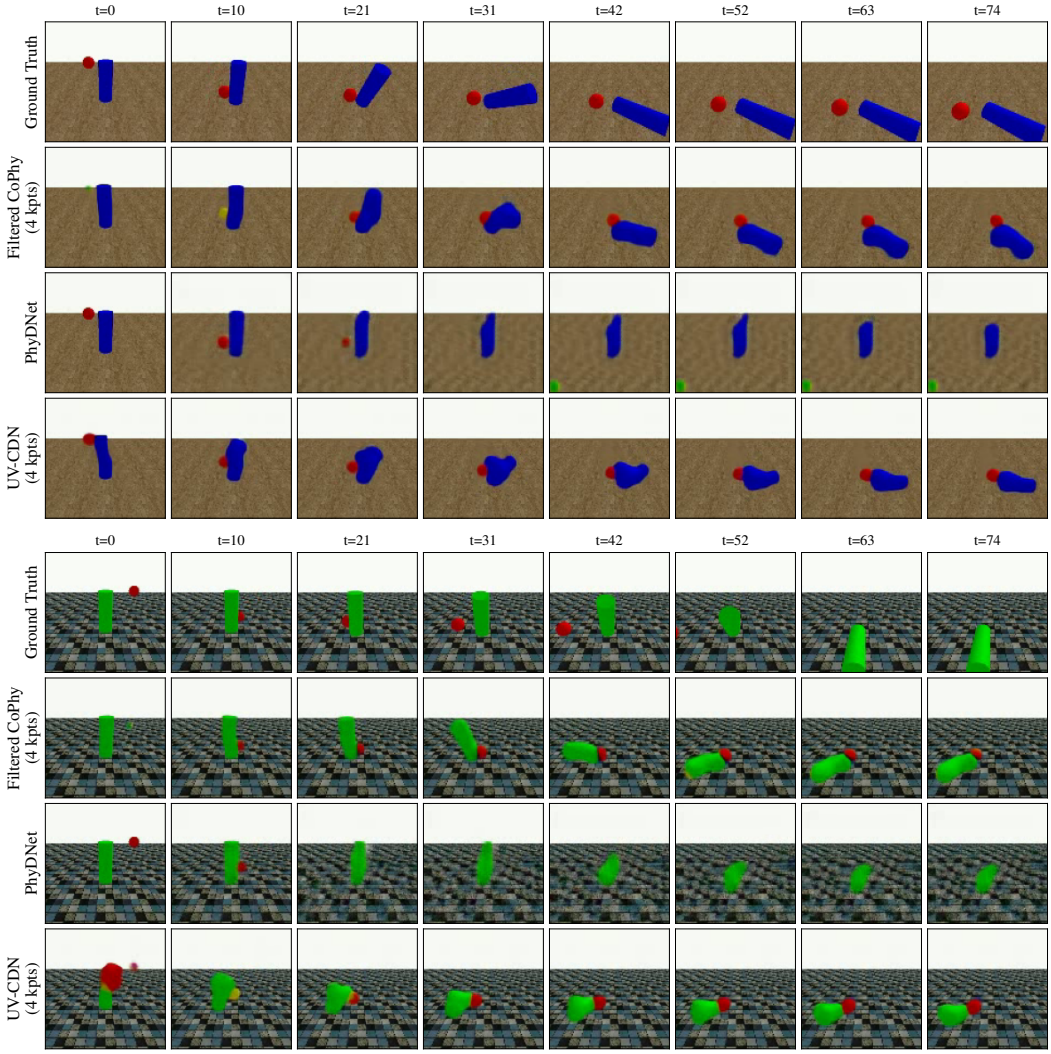

Figure 18: The CoPhy benchmark suite is subdivided in three scenarios involving 2D or 3D rigid body dynamics with complex interactions, including collision and resting contact.